Enhancing ZnO-based supercapacitors through carbon-induced defect centers

Egehan Ercay,† Serra Ersoy,† Mucahid Ozcan, Feray Bakan Misirlioglu, Ahmet Gungor, Andrew Ozarowski, Figen Kaya, Arpad Mihai Rostas,* Cengiz Kaya,* and Emre Erdem*

Accepted: 11 December 2024

This study explores the effects of eco-friendly reducing and capping agents on synthesizing zinc oxide (ZnO) nanoparticles for use as electrode materials in supercapacitors. The researchers successfully produced ZnO nanoparticles with different sizes and shapes using a sol–gel method and four different capping agents: tartaric acid, chitosan, ascorbic acid, and hydroxybenzoic acid. The properties of the ZnO nanoparticles were thoroughly examined through morphological, structural, and electrochemical studies. The defect structure of the materials was analyzed using photoluminescence spectroscopy, while electron paramagnetic resonance spectroscopy revealed the presence of carbon-based signals related to doping the host material with carbon during synthesis. Specific capacitance measurements indicated that supercapacitors using the C-doped ZnO nanomaterial as electrode materials demonstrated potential for energy-storage applications. Specifically, when tartaric acid was used as a capping agent, the maximal specific capacitance, energy density, and power density values reached 103.1 F/g, 14.3 Wh/kg, and 167 kW/kg, respectively. These results show promise for the development of next-generation supercapacitor devices based on ZnO.

Impact statement

This article aims to elucidate the impact of eco-friendly reducing and capping agents used in the synthesis procedure of zinc oxide nanoparticles employed as electrode materials in supercapacitor applications. ZnO nanoparticles were successfully synthesized by a sol–gel method with four different capping agents: tartaric acid, chitosan, ascorbic acid, and hydroxybenzoic acid. Thorough morphological, structural, and electrochemical studies were conducted to elucidate their properties. Photoluminescence spectroscopy distinguished dominant defect structures inside the nanomaterials. At the same time, electron paramagnetic resonance spectroscopy analyzed the intrinsic and extrinsic paramagnetic defect structures, revealing the presence of carbon-based signals related to doping the host material with C during the synthesis procedures. Specific capacitance measurements were performed, which showed that symmetrical supercapacitors using the C-doped ZnO nanomaterial as electrode materials have great potential in energy-storage applications. The maximal specific capacitance, energy density, and power density values obtained reached 103.1 F/g, 14.3 Wh/kg, and 167 kW/kg, respectively, when tartaric acid was employed as a capping agent. The results are promising compared to the literature and could be a starting point in developing new-generation supercapacitor devices based on carbon-doped ZnO.

Introduction

Energy-storage systems such as supercapacitors (SCs) have gained growing significance in electric cars, computers, and electronic devices. SCs hold promise as energy-storage devices, owing to their remarkable specific power and extended cycling life.[1,2] In addition, nanotechnology has an important impact on SC applications.[1,3–5] Metal oxides contribute to the electrodes' specific capacity and energy density, while carbon nanostructures optimize their power density and cycling life. An effective technique to improve electrochemical performance is the hybridization of carbon materials with different metal oxides, such as NiO, FeO_x, and ZnO.[6–8] ZnO nanoparticles are often used in this

Egehan Ercay, Department of Materials Science and Nano Engineering, Faculty of Engineering and Natural Sciences, Sabanci University, Istanbul, Turkey
Serra Ersoy, Department of Materials Science and Nano Engineering, Faculty of Engineering and Natural Sciences, Sabanci University, Istanbul, Turkey; Department of Metallurgical and Materials Engineering, Faculty of Chemistry and Metallurgy, Yildiz Technical University, Istanbul, Turkey;
Mucahid Ozcan, Department of Metallurgical and Materials Engineering, Faculty of Chemistry and Metallurgy, Yildiz Technical University, Istanbul, Turkey; Department of Metallurgical and Materials Engineering, Adiyaman University, Adiyaman, Turkey;
Feray Bakan Misirlioglu, Department of Materials Science and Nano Engineering, Faculty of Engineering and Natural Sciences, Sabanci University, Istanbul, Turkey
Ahmet Gungor, Department of Materials Science and Nano Engineering, Faculty of Engineering and Natural Sciences, Sabanci University, Istanbul, Turkey
Andrew Ozarowski, National High Magnetic Field Laboratory, Florida State University, Tallahassee, USA
Figen Kaya, Department of Metallurgical and Materials Engineering, Faculty of Chemistry and Metallurgy, Yildiz Technical University, Istanbul, Turkey
Arpad Mihai Rostas, Physics of Nanostructured Systems, National Institute for Isotopic and Molecular Technologies, Cluj-Napoca, Romania; arpad.rostas@itim-cj.ro
Cengiz Kaya, Department of Metallurgical and Materials Engineering, Faculty of Chemistry and Metallurgy, Yildiz Technical University, Istanbul, Turkey; cengizk@yildiz.edu.tr
Emre Erdem, Department of Materials Science and Nano Engineering, Faculty of Engineering and Natural Sciences, Sabanci University, Istanbul, Turkey; emre.erdem@sabanciuniv.edu
*Corresponding author
†Egehan Ercay and Serra Ersoy contributed equally to this work.
doi:10.1557/s43577-024-00845-z

field due to their exceptional qualities, including anticorrosion, excellent heat resistance, high thermal and chemical stability, good oxidation resistance, ultraviolet protection, high refractive index, low cost, high theoretical energy density, and high conductivity.[9] At the same time, it was observed that ZnO nanoparticles have low optical pumping threshold values and radiation resistance.[10,11] ZnO has been used in optoelectronics with its extraordinarily broad bandgap (3.37 eV) and substantial exciton binding energy (60 meV) at ambient temperature.[12] A wide bandgap offers several advantages, including high breakdown voltages, the ability to sustain substantial electric fields, reduced electronic noise, and the capability to handle high temperatures, and power levels. ZnO typically exhibits *n*-type characteristics. Its cost-effectiveness, biocompatibility, and ecological safety make it highly promising as an SC electrode material. Compared to many other transition-metal oxides, including CoO (715 mAh/g), NiO (718 mAh/g), and CuO (674 mAh/g), ZnO has a greater theoretical capacity (978 mAh/g). It is a great material for solid-state white illumination due to its high emission efficiency[13] and large gap, which requires ultraviolet light (387 nm) for activation.[14] ZnO's hydrophilic and photocatalytic processes usually occur in practical applications, which could result in the hydrophilic self-cleaning or photocatalytic effect.[15] In addition, it can be applied to photo printing, protective coatings, solar cells, blue laser diodes, SCs, conductive thin-film liquid-crystal displays (LCDs), and electrophotography.[16]

Furthermore, paramagnetic centers are crucial in SCs based on ZnO.[17] They are associated with ionized oxygen or zinc vacancies that appear in the ZnO crystal structure, significantly influencing the performance of the SC by affecting their charge-storage capacity and electrical conductivity. These properties can be effectively studied and manipulated using electron paramagnetic resonance (EPR) spectroscopy, thereby optimizing the performance of the SC. EPR is an effective tool for investigating defect centers at the atomic level. The association of EPR and optical spectroscopies, thus, enables a more comprehensive understanding of the defect structures broadly and specifically in the case of ZnO. Four types of defect centers can exist in ZnO: zinc/oxygen vacancies and zinc/oxygen interstitials. Zinc interstitials are diamagnetic, meaning EPR cannot detect them.[18] On the other hand, depending on their electron configuration, oxygen interstitials can be paramagnetic and thus detectable by EPR.

The particles' size, porosity, and electrical structure significantly influence the sensing capabilities of metal oxide in energy-storage applications.[19] High surface area, chemical and photochemical stability, homogeneity in pore size, shape selectivity, and rich surface chemistry are just a few of the benefits of porous ZnO. A large surface area of porous ZnO increases surface activity.[20] The amount of porosity is directly affected by the synthesis technique. Various techniques are employed for nanoparticle synthesis, such as the sol–gel process, coprecipitation, green synthesis, the hydrothermal process, and combustion synthesis. Compared to the other methods described, the sol–gel process is the most widely used due to its high-purity product, excellent chemical homogeneity, low sintering temperature, ease of morphology control, low cost, atomic mixing, and reduced environmental risk.[21]

Carbon incorporation into metal oxides can significantly improve the electrical conductivity of the electrode material, having excellent electron-transport properties. When combined with metal oxides, which typically have poorer conductivity, the composite material allows for more efficient charge transfer.[22] The high surface area is crucial for SCs as it provides a greater charge to be stored. Carbon materials are known for their vast surface areas, and when doped into metal oxides, they can create a synergistic effect that enhances the overall capacitance of the SCs.[23] The structural robustness of carbon materials helps maintain the integrity of metal oxides during the repeated charge–discharge cycles of an SC. The increased durability translates into longer lifetimes and better performance reliability.[24,25]

Combining carbon defects with metal oxide can lead to synergistic effects where the total electrochemical performance exceeds the sum of its parts. For example, carbon can provide high conductivity and surface area, whereas metal oxide can contribute to specific capacitance through redox reactions. Some carbon-based defects can contribute to pseudocapacitance by participating in reversible redox reactions, an additional charge-storage mechanism alongside the electric double-layer capacitance. These points illustrate how carbon doping and the associated defective structures enhance the electrochemical properties of metal oxides for SCs.[3]

Chitosan is a naturally occurring cationic biopolymer with exceptional charge-storage capacity and can be used as a binder. It has a high concentration of amino groups (−NH2) as well as hydroxyl (−OH) groups that increase its ability to interact with metal ions through ion exchange and electrostatic attraction.[26] Tartaric acid ($C_4H_6O_6$) was utilized in this work as the structure-directing agent to change the surface of ZnO particles because it is extremely water soluble and can easily couple with Zn^{2+} ions.[9,11,16] Ascorbic acid ($C_6H_8O_6$) salt, a plant-based reagent, was used as the corresponding redox molecules. Due to the presence of ascorbic acid, metal ions could be maintained in solution during the process.[27,28] Hydroxybenzoic acid ($C_7H_6O_3$) is widely used in the synthesis of emulsifying agents, antioxidants, corrosion inhibitors, and food preservatives as reducing and capping agents.[29]

The synthesis of zinc oxide nanoparticles via the sol–gel method used various capping agents, including tartaric acid, acetic acid, ascorbic acid, and hydroxybenzoic acid. These agents, through their functional groups, facilitated the transformation of the solution into a gel upon heating, leading to the formation of zinc oxide nanoparticles.[10] The electrochemical performance of these materials is significantly influenced by their porous nature, which facilitates rapid proton exchange without degrading the electrode's

performance. The most effective electrochemical results were observed with the porous zinc oxide nanoparticles synthesized using tartaric acid.[13] The functional groups, such as carboxylic acid (in tartaric acid), can chemically bind to the surface of ZnO nanoparticles, changing the electronic environment of the ZnO surface and potentially creating more active sites for the adsorption of electrolyte ions. It can also increase the hydrophilicity of ZnO nanoparticles. Improved wettability ensures that the electrolyte can easily penetrate the pores and come into contact with the surface of the nanoparticles, which is crucial for maximizing capacitance.[30] Benzene rings contain delocalized π-electrons, which can interact with the π-electrons of other aromatic structures or conjugated systems. These π–π interactions can facilitate charge-transfer processes within or between the material and the electrolyte. As observed with hydroxybenzoic acids, the presence of benzene rings can influence the size of the nanoparticles. Smaller nanoparticles have a higher surface-to-volume ratio, which could provide more active sites for charge storage. Benzene rings can potentially create more conductive pathways within the ZnO structure, improving the electronic conductivity of the material and leading to a faster charge and discharge process, which is desirable in supercapacitors.[31] The presence of carboxylic acid and benzene ring functional groups on ZnO nanoparticles can significantly influence the capacitance of supercapacitors by affecting the surface area, porosity, wettability, conductivity, and stability of the electrode material. These modifications enhance the supercapacitors' energy-storage capacity and efficiency by optimizing the interaction between the active material and the electrolyte.

Unlike current materials, which are not environmentally friendly, these capping agents are bio-based and sustainable.[32,33] This study also introduces an eco-friendly sol–gel method for synthesizing ZnO nanoparticles, an approach that enhances the materials properties by creating distinct nanoparticle morphologies and carbon-induced defect centers, a technique not widely explored for supercapacitor applications.[21] Notably, the discovery of oxygen vacancies contributing to a strong green emission profile can simplify future assessments of electrochemical behavior, reducing extensive testing needs. Overall, this research demonstrates that superior electrochemical properties can be achieved with eco-friendly methods and materials, paving the way for innovations in green energy storage while maintaining sustainability.

Thus, zinc sources of zinc acetate dihydrate and zinc nitrate tetrahydrate were utilized with tartaric acid, chitosan, ascorbic acid, and hydroxybenzoic acid in sol–gel nanoparticle production to assess their effect on the crystal formation and therefore on the size and morphology of synthesized zinc oxide, and their impact was studied concerning their electrical properties and their potential to be used as electrode materials for SC applications.

Materials and methods

The following materials were used in the synthesis procedures of the ZnO materials: zinc nitrate tetrahydrate (Merck 108833 for analysis Emsure), zinc acetate dihydrate (Merck 108802 for analysis Emsure), tartaric acid (Merck 100804 L (+) for analysis Emsure), chitosan (448869 low-molecular-weight Emsure), 4-hydroxybenzoic acid (ReagentPlus, ≥ 99% Emsure), and ascorbic acid (Merck 100468 L (+) ascorbic acid for analysis Emsure) from Sigma-Aldrich. Acetic acid was used as a solvent.

ZnO-based powder samples were synthesized by the sol–gel method using various zinc sources combined with reagents (additives) used as reducing and capping agents. In the following, the process steps of the synthesis of each sample are described. ZA/TA: zinc acetate (ZA) dihydrate was dissolved in 100-ml distilled water (DW) in a 250-ml beaker, and tartaric acid (TA) was added dropwise to the solution. The prepared solution was mixed in a magnetic stirrer for 1 h until the temperature reached 90°C. The solution was then dried at 80°C for 24 h and calcinated at 500°C for 1 h in a muffle furnace. Similar process steps were followed for the ZN/TA sample, except the starting zinc source was zinc nitrate (ZN) tetrahydrate. For the ZA/Ch sample, chitosan (Ch) and zinc acetate dihydrate were added separately to 100 ml of DW and mixed. Then, 1 ml of acetic acid was added dropwise into the mixture and stirred until a homogeneous mixture was obtained. Finally, the solution was centrifuged twice at 4000 rpm for 10 min to filter out precipitated particles. The separated powders were then dried and calcined as before. For the ZA/AA sample, ascorbic acid (AA) and zinc acetate dihydrate solutions were prepared separately, and the ascorbic acid was added to the zinc acetate solution dropwise. For the ZA/HBA sample, a hydroxybenzoic acid (HBA) solution was added to the zinc acetate solution dropwise, followed by drying and calcination steps. Finally, the five powder samples were ground using an agate mortar. The experimental procedures followed are summarized in the Supplementary information (SI) Scheme S-Synth[†].

The selection of tartaric acid for testing with both zinc precursors was based on its distinctive characteristics that promote the development of porous and rod-shaped ZnO structures.[34] The objective of the work was to investigate the impact of the zinc supply on the morphology and electrochemical characteristics when TA is employed as the capping agent. This investigation yielded a valuable understanding of the precursor's function in the synthesis procedure and its influence on the resultant material characteristics. The selection of the capping agents, chitosan (Ch), ascorbic acid (AA), and hydroxybenzoic acid (HBA), was based on their unique chemical characteristics and ability to include carbon-induced defect sites.[32,35] Each agent contributes to the shape and defect structure of the ZnO nanoparticles. For example, chitosan is a biopolymer with a large capacity for storing charges,[33] ascorbic acid is a redox molecule derived from plants,[36] and hydroxybenzoic acid is recognized for

its ability to reduce and cap carbon.[37] Each of these compounds was evaluated using zinc acetate to investigate their specific impact on the production and functionality of ZnO nanoparticles.

X-ray diffraction (XRD) measurements were carried out with a Malvern PANalytical X-Pert PRO diffractometer system. XRD patterns were obtained in an angular range of 2θ = 20–80°, with a scan rate of 1°/min. The diffractometer utilized CuKα1 radiation, which has a wavelength λ = 1.54059 Å and a generator voltage of 60 kV. Scanning electron microscopy (SEM) is a technique for testing micro areas and understanding microstructures. A ZEISS Sigma 300 VP SEM microscope with an accelerating voltage of 3–5 kV was used. Examining the lattice dynamics of ZnO nanostructures at the molecular level was made possible by applying Raman spectroscopy. The Renishaw Raman inVia System, combined with a 532-nm green laser, was employed to conduct these measurements. This advanced analytical technique allowed for a detailed examination of the molecular interactions within the ZnO nanostructures. Photoluminescence (PL) spectroscopy was employed to collect crucial information about structural defects of the materials, using an Edinburgh Instruments FS5 spectrofluorometer to understand the optical properties. A 320-nm excitation wavelength was used at room temperature with a slit distance for excitation and emission of 5 and 10 nm, respectively. Electron paramagnetic resonance (EPR) spectroscopy measurements were carried out on a Bruker E-500 ELEXSYS X-band (9.88 GHz) and Q-band (33.4 GHz) spectrometer at room temperature under identical conditions using equal quantities of samples. The high-field EPR spectra were obtained at a frequency of 406.4 GHz using the EMR facility at NHMFL, which employs a custom-built spectrometer. This transmission-type instrument, devoid of a resonance cavity, utilizes cylindrical light pipes to propagate waves. Microwave generation was accomplished through a phase-locked oscillator (Virginia diodes) operating within the 8–20-GHz range. This frequency was then multiplied through a chain of frequency multipliers, yielding the 2nd, 4th, 8th, 16th, 24th, 32nd, and 48th harmonics. The frequency precision exceeds seven significant digits. An Oxford Instruments superconducting magnet capable of producing a 17 T field was utilized. Modulation was set at 50 kHz alongside amplitude values of 5 and 10 G, though these are approximate due to instrument constraints.

To measure the electrochemical properties of the powder samples based on ZnO, symmetric SCs were prepared. The SC design used during this study consists of two electrodes, a separator, and an electrolyte. All symmetric SCs were prepared with 3 mg of electrode material, a 6 M KOH electrolyte, and a glass fiber separator. A biologic VMP 300 multipotentiostat was used for all of the following analyses: cyclic voltammetry (CV), electrochemical impedance spectroscopy (EIS), and galvanostatic cycling with potential limitation (GCPL). CV was conducted using various scan rates ranging from 1 to 200 mV/s within a voltage range of 0–1 V, which was set considering water electrolysis at 1.23 V. GCPL analysis involved an assessment of SC specific capacity (mAh/g), Coulombic efficiency (%), and capacitance retention (%) values. GCPL analysis was performed within the voltage window 0–1 V.

Results and discussion

The XRD patterns of the synthesized ZnO-based materials are displayed in **Figure 1**a and indexed according to the JCDPS card no 36 1451, confirming the hexagonal wurtzite structure with peaks related to the (100), (002), (101), (102), (110), (103), (200), (112), (201), (004), and (202) atomic planes, characteristic of ZnO nanoparticles.[38] The degree of crystallization calculated based on Rietveld refinement (see Figure 1b) for each sample is given in **Table I**, showing that the highest crystallinity is observed for the ZA/HBA sample, which carbon elevation in composition could cause.[16,38]

The structural stability of the ZA/HBA nanoparticles is attributable to their well-ordered atomic arrangement within the crystal lattice, as evidenced by their high crystallinity. Furthermore, Rietveld refinement data revealed that ZA/HBA possessed the greatest average crystallite size and the highest degree of crystallinity. In contrast to the ZA/HBA sample, the decreased average crystallite size of the ZN/TA samples, as determined by Rietveld refinement data, results in a less regular atomic structure and the potential for defect centers to manifest.

The high-resolution SEM images taken at low magnifications show that ZA/TA and ZN/TA exhibit rod-like structures with extensive porosity between the grains, as shown in **Figure 2**a and b. However, a closer inspection at higher magnification (see the inset of Figure 2) reveals that the ZA/TA sample contains a mixture of micrometer-sized spheres and very fine equiaxed nanostructures, also showing the extent of the porous structures in the ZN/TA sample. Porous structures could enhance electrochemical activity by providing a more active surface. SEM micrographs demonstrate that the addition of TA creates rod-like structures independent of the Zn source, probably due to alteration of the polar planes of the ZnO crystal with the addition of TA, which could cause preferential growth.[34] In the literature, TA has been reported to function as a structure-directing agent. It is reported that lateral growth is favored at low TA concentrations, leading to either a hexagonal or spherical structure formation.[34] In contrast, directional growth is favored for high concentrations of TA, where smooth one-dimensional structures are formed.[39,40] Figure 2c shows that combining ZA with Ch leads to micron-sized globular ZnO structures due to the presence of the hydroxyl groups, where at higher magnification, nano-sized spherical crystals are observed on the surfaces of the globes. On the other hand, using AA and HBA promotes the formation of nanometric feather-like fibrous structures, as shown in Figure 2d and e.

Raman spectroscopy provided insight into the lattice dynamics of the ZnO nanostructures at a molecular level. The spectra in **Figure 3** demonstrate the successful synthesis of

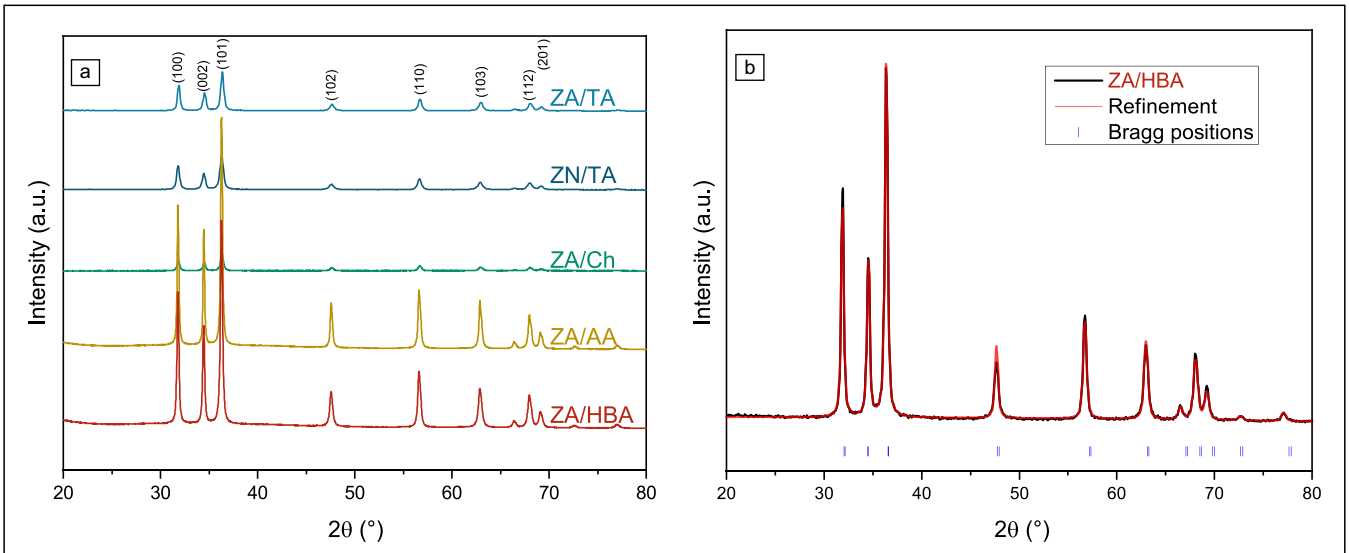

Figure 1. X-ray diffraction patterns of the ZnO materials obtained with different capping agents showing the atomic planes of the hexagonal wurtzite structure characteristic for ZnO nanoparticles (a) and Rietveld refinement results of the ZA/HBA sample (b).

Table I. Crystalline (CR), amorphous (AM) phases of the different ZnO nanoparticles, and the average crystallite size (ACR) calculated from the Rietveld refinement.

Sample	CR/%	AM/%	ACR/nm^3
ZA/TA	83.6	16.4	48.1
ZN/TA	82.3	17.7	41
ZA/Ch	81.7	18.3	85
ZA/AA	83.7	16.3	93
ZA/HBA	84.2	15.8	71

ZnO using various starting materials, excluding chitosan. The number of phonons in the hexagonal wurtzite (P63mc) ZnO structure varies according to the number of atoms in the unit cell, with 12 phonons, including three acoustic.[41] A prominent peak around 430 cm^{-1} is ascribed to the E_{2high} mode of ZnO, serving as a distinctive Raman signature for wurtzite ZnO. The E_{2low} mode remained undetected, but the vibration occurring at approximately 320 cm^{-1} is typically associated with a second-order Raman process and is attributed to the $E_{2high} - E_{2low}$ difference mode.[42] In the wurtzite structural configuration, the A_1 and E_1 phonon modes experience a divergence, resulting in the emergence of transverse optical (TO) and longitudinal optical (LO) phonons, a consequence of the inherent polarity of the structure.

The activation of the TO modes hinges on the alignment of incident and scattered light perpendicular to the *c*-axis. In contrast, LO phonon modes manifest when incident and scattered light align parallel to the *c*-axis. In particular, a subdued peak around 570 cm^{-1} is ascribed to the A_1(LO) mode. In cases where the material's structure contains surface and/or aggregate defects, a second-order Raman process could ensue, leading to the appearance of combination bands that encapsulate the summation of frequencies stemming from the optical branches. Within this context, two-phonon difference modes are confined within the frequency range of single-phonon branches.

In contrast, frequencies that exceed the approximate threshold of 600 cm^{-1} are governed by two-phonon sum modes and higher-order multiphonon processes, as elucidated in Figure 3.[43,44] In addition to the aforementioned spectral features, we have observed two distinct characteristics within the synthesized samples. These observed features are the carbon traces that originate in the starting chemicals and are presumed to originate in the sp_2 carbon domains, possibly representing unbound carbon elements within the samples. The presence of the G-band at 1590 cm^{-1} indicates C–C bond stretching, a defining attribute of sp_2 carbon systems that form rings and chains. Conversely, the emergence of the D band around 1350 cm^{-1} is contingent upon sp_2 carbons within disordered ring structures, and its manifestation is influenced by the composition and arrangement of these sp_2 carbon elements, as noted in previous studies.[42,43]

The defect structure of the ZnO-based materials was further investigated by PL and EPR spectroscopy. **Figure 4**a shows the PL spectra of all synthesized samples, which were deconvoluted to represent the peaks in different emission regions. As depicted in Figure 4b and SI S-PL[†], they all demonstrate defective structures in the visible light range.

The first peak observed in all of the samples, around 390 nm, corresponds to the bandgap energy of the samples. This peak is mostly attributed to the e-—h$^+$ recombination and is named near band edge (NBE).[45] The following broad peak at the visible light range is associated with the structural

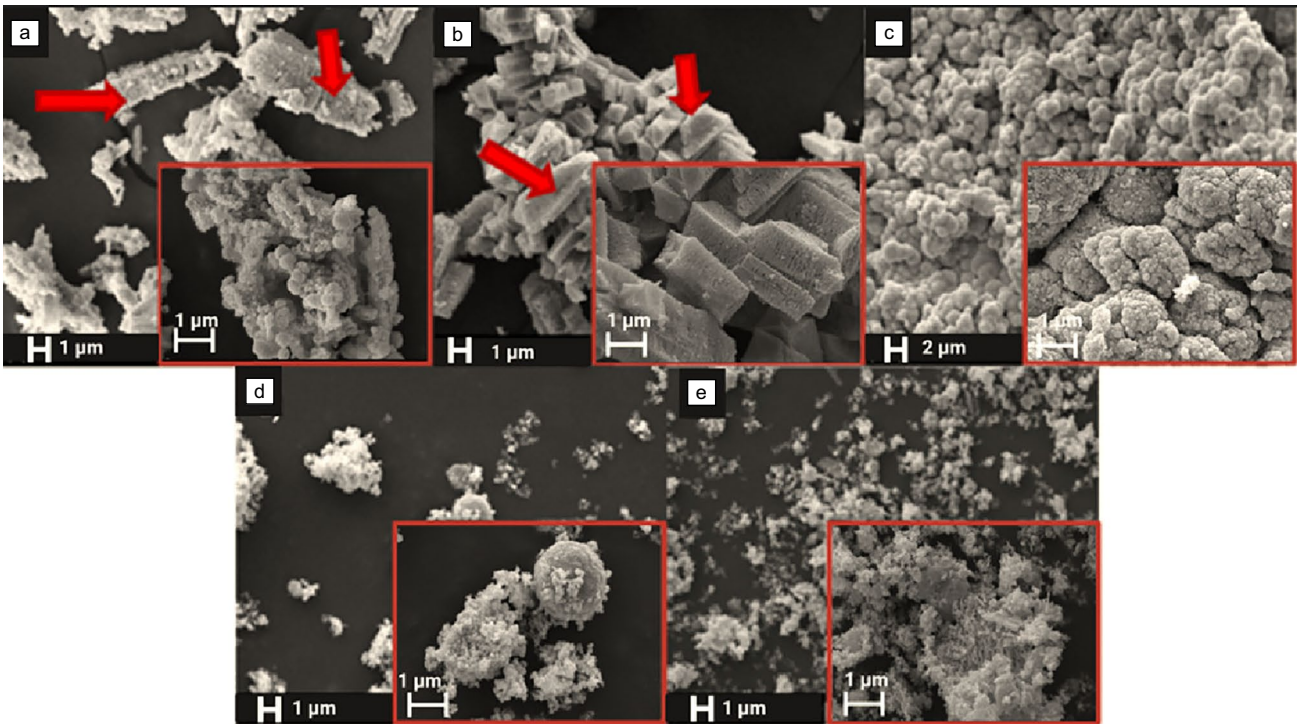

Figure 2. Scanning electron microscopy micrographs of the ZnO-based materials: ZA/TA (a), ZN/TA (b), ZA/Ch (c), ZA/AA (d), and ZA/HBA (e) at two different magnifications, depicting the morphology changes induced by the reducing and capping agents used in the synthesis of the materials.

defects expected in ZnO-based samples. The bandgap energy, which varies from material to material, can be calculated with $E_g = \frac{h \cdot c}{\lambda}$, where E_g corresponds to the bandgap energy, h is Planck's constant, c is the speed of light, and λ is the wavelength of the PL peak. The typical ZnO-based sample's bandgap energy is around 3.1–3.4 eV. The bandgap energy of all ZnO-based samples was calculated and found to be ~3.2 eV using the peak around 390 nm. PL analysis of ZnO reveals intriguing insights into its defect structures, particularly evident through emissions in the visible light spectrum. The presence of intrinsic defects such as zinc interstitials (Zn_i), vacancies (V_{Zn}), oxygen interstitials (O_i), and vacancies (V_O) contributes significantly to these emissions. In particular, samples with prevalent oxygen vacancies exhibit a distinctive green emission profile.[46] This emission is attributed to the hexagonal core of ZnO nanocrystals, where negatively charged Zn vacancies function as shallow acceptors, delineating a fascinating aspect of ZnO defect engineering via PL studies.

Multifrequency EPR measurements were performed to better comprehend the origin of the defect centers in the ZnO-based materials. X-band measurements performed at an excitation microwave frequency of 9.88 GHz (**Figure 5**a) revealed the usual ZnO-related core–shell EPR signals.[45,47,48] with characteristic g-values of ~2.005 and 1.96. As presented in previous studies, the EPR signal with $g \approx 1.96$ arises from

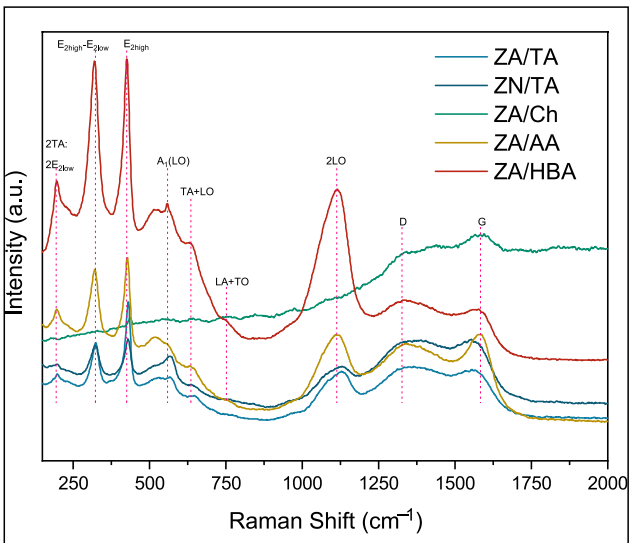

Figure 3. First-order and second-order Raman spectrum of the synthesized particles (λ = 532 nm). The vibration bands' alterations in the 125–2000 cm^{-1} range are given.

the hexagonal core of the ZnO nanocrystal due to negatively charged Zn vacancies acting as shallow acceptors.[18] In contrast, the EPR signal with $g \approx 2.005$ was assigned to a shell

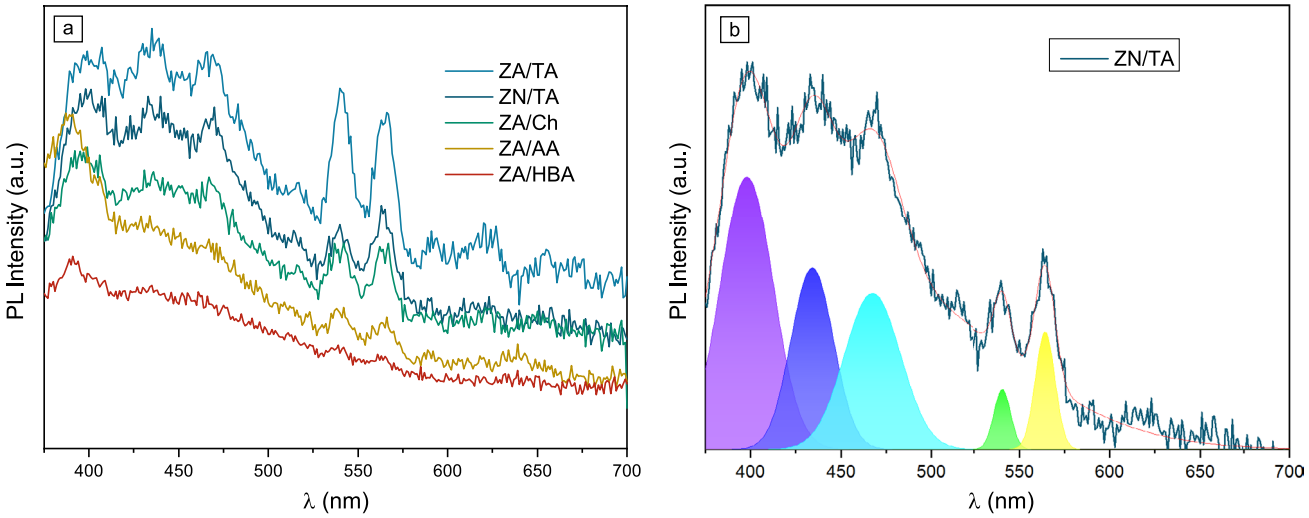

Figure 4. Photoluminescence (PL) spectra of the ZnO-based materials obtained with different capping agents (a), and the deconvolution of the ZN/TA PL spectrum (b) representing the peaks in different emission regions, demonstrating defective structures with emissions in the visible light range.

environment containing a high concentration of surface defects identified as positively charged oxygen vacancies acting as deep donors.[49] The shell-based paramagnetic signals usually appear in nano-sized ZnO materials,[45] which is not the case in the present materials simply judging by the SEM images presented in Figure 2.

Thus, to elucidate the origins of the EPR signal at lower magnetic fields, further EPR measurements in the Q-band that operates at 33.4 GHz were carried out. As presented in Figure 5b, compared to the X-band measurements, the EPR signal with $g \approx 2.005$ broadens, indicating the presence of anisotropies or an additional paramagnetic center that is not ZnO-related. Still, the resolution was not high enough to separate the signals from each other.

Ultrahigh-field EPR measurements were performed at 406.4 GHz to solve this issue. Figure 5c presents the EPR spectra of the ZN/TA and ZA/HBA samples, revealing the third EPR signal with a *g*-value of 2.0021, along with the presence of the ZnO-related core–shell signals already discussed. Regarding the synthesis method and the presence of the capping agents, we assume that this new signal is related to carbon centers, which entered the system as an intrinsic dopant. Previous studies report similar *g*-values for carbon-related defect centers. Raman measurements have verified the existence of a carbon signal, and typical G and D band signals due to graphitic and defective carbon have been observed (see Figure 3). The EPR signal of carbon nanoparticles,[50] nanotubes,[51] and nanoparticles[52] in ZnO has been intensively investigated, where various relaxation mechanisms were presented to form C paramagnetic centers in ZnO after synthesis parameters, such as mechanical activation or grinding chamber. Similar carbon formation can be introduced here via different reagents.

Electrochemistry is essential in surface and analytical sciences because it enables the measurement of current or potential to evaluate the reactivity of the working electrode. It also allows for altering current or potentials to modify the interface properties, ranging from atomic or molecular level to macroscopic films. EIS is a highly appropriate method to analyze different processes in response to a small stimulus applied to the interface.[53] **Figure 6** displays the Nyquist curves of the SCs fabricated with ZnO nanoparticles as electrodes. The Nyquist curves of each SC exhibit the same pattern, resulting in similar $-\mathbb{Z}_{im}$ and $\mathbb{Z}_{re}$ values. Upon analysis of the Nyquist curve, it becomes apparent that SCs prepared with Ch as capping agents exhibit higher $\mathbb{Z}_{re}$ values, indicating a greater energy loss due to greater resistance.

TA, Ch, and AA nanoparticles have significantly higher $-\mathbb{Z}_{im}$ values, indicating that the inductive effect dominates the capacitance components, resulting in elevated inductance. The intersection of the Nyquist curve with the x-axis corresponds to the resistance of the equivalent circuit, also known as the ohmic resistance, which quantifies the energy losses resulting from the electrical resistance between the electrode and the electrolyte.[54,55] The inset of Figure 6 depicts the ohmic resistances of each SC. The ohmic resistances for ZA/AA, ZA/Ch, ZA/HBA, ZA/TA, and ZN/TA were determined as 1.6, 1.02, 8.87, 0.75, and 1.18 Ω, respectively.

CV is a technique for investigating the charge-storage process, determining the optimal voltage range, and studying the kinetics in SCs.[56] As the scan rate increases, the detected current also increases for all SCs, indicating the favorable stability of the electrode materials (see **Figure 7**). The SC assembled with ZA/Ch exhibits the highest current, followed by ZA/AA and ZN/TA when the scan rate is 200 mV/s. In the

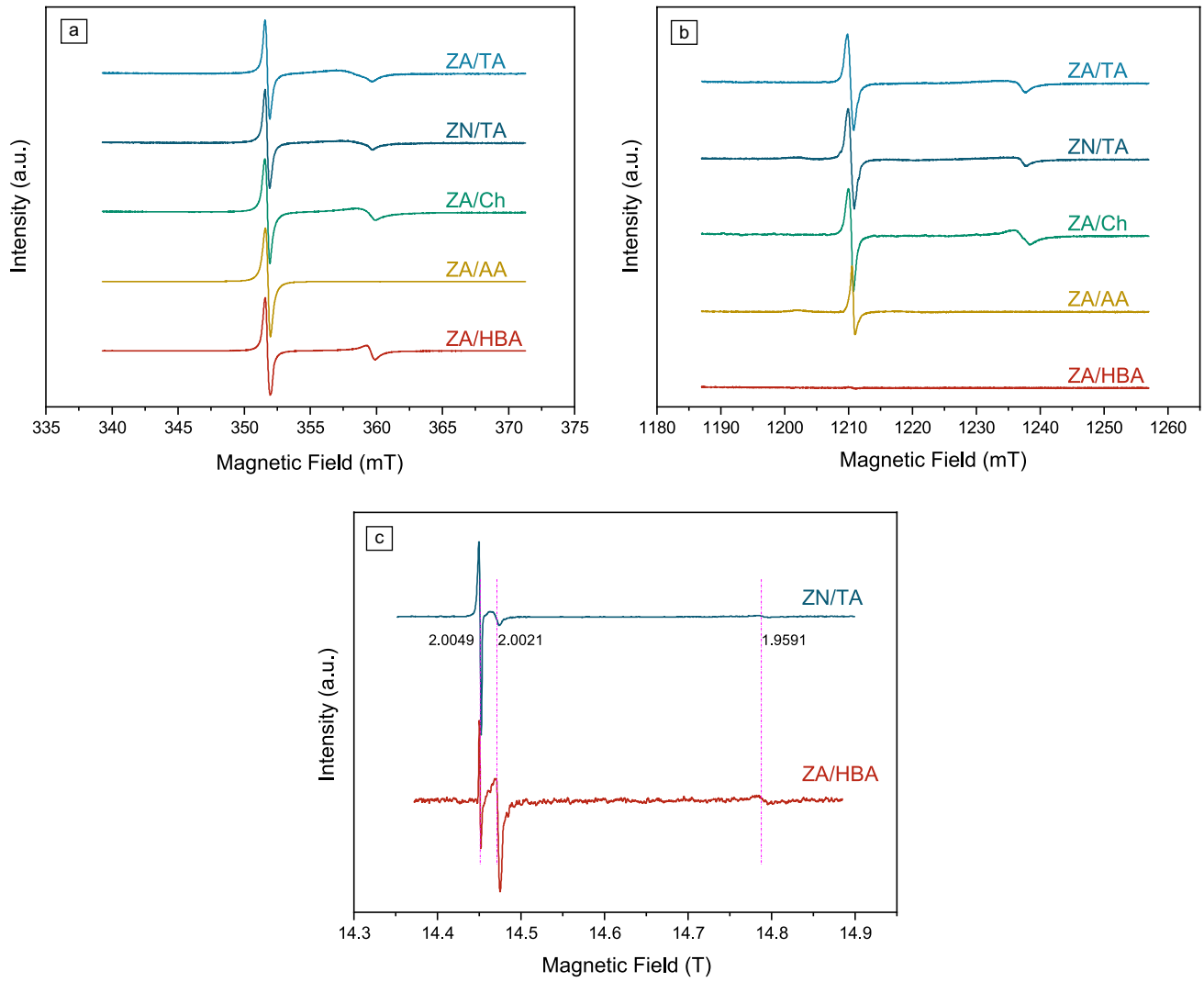

Figure 5. Electron paramagnetic resonance (EPR) spectra of the ZnO samples synthesized with different capping agents measured in X-band –9.88 GHz (a), Q-band –33.4 GHz (b) exhibiting ZnO-related core–shell EPR signals with characteristic *g*-values of ~2.005 and 1.96, and high-field –406.4 GHz (c) revealing a third C-related EPR signal with a *g*-value of 2.0021.

analysis of ideal SCs, a rectangular shape is expected to be observed in the CV analysis.[57] Upon comparing the CV shapes obtained from the SCs, it is evident that there is a deviation from the expected capacitive behavior. Instead, a pseudocapacitive behavior is observed, characterized by the absence of distinct redox peaks.[58] Our study utilized a 6 M KOH solution as an electrolyte. KOH undergoes decomposition in a manner analogous to that of water, producing hydrogen gas and hydroxide ions. The dissociation process begins when the electrode potential reaches a negative value, especially at a voltage of approximately −1.23 V; it is frequently possible to observe the separation of water molecules and, consequently, the separation of KOH. As previously observed in other studies,[57,59] KOH can undergo decomposition at positive potentials greater than 0.8V. Upon examining the CV curves, it becomes evident that the water separation is only partial, allowing measurements to be taken within the 0–0.8 V range. However, electrochemical experiments were conducted with voltage windows ranging from 0 to 1 V to assess the performance and capabilities of the designed supercapacitors fully.

The integral of the CV curve corresponds to the amount of energy produced in the region of high voltage and low current resulting from a redox reaction in the electrochemical cell.[60,61] This area assesses the electrochemical performance of the electrode material and represents its energy-storage capability. While ZA/Ch showed the highest current value at a scan rate of 200 mV/s, ZA/TA and ZN/TA exhibited the highest field at a scan rate of 1 mV/s.

Specific capacitance values (C_P) were determined at different scan rates. The results obtained are shown in **Figure 8**.

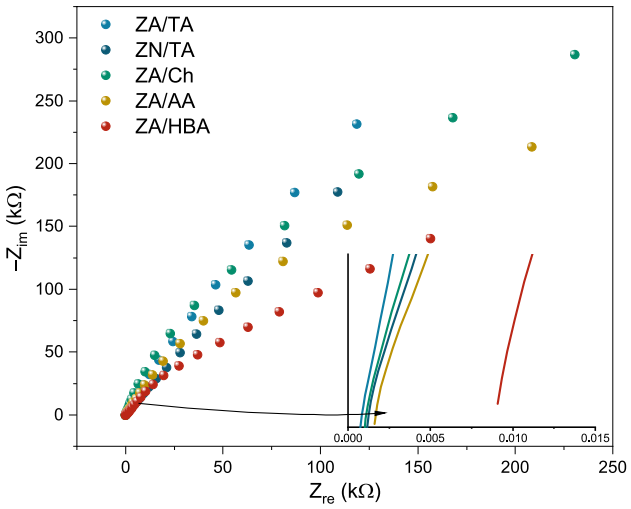

Figure 6. Potentio electrochemical impedance spectroscopy measurement results for the ZnO-based supercapacitor materials. The inset evidences *x*-axis intercept, which represents the ohmic resistance of the system.

The scan rate significantly influences the specific capacitance in CV analysis, influencing diffusion processes, electrochemical reaction kinetics, and double-layer capacitance. A slower scan rate promotes the efficiency of electrochemical reactions and ion diffusion processes. Slow scanning contributes to increased diffusion of ions on the electrode surface and a more even distribution of charges across the electrode, increasing the number of ions interacting with a greater amount of active material, thus increasing the specific capacitance.[62] In addition, a slower scan rate could allow enhanced charging of the double-layer capacitance at the interface between the electrode and electrolyte, promoting more controlled charging and discharging of the electrode surface.[62,63] The described situation is also seen in Figure 8, where it is observed that the specific capacitance shows a substantial increase as the scanning rate decreases from 200 to 1 mV/s.

The GCPL analysis was used to characterize the SC devices' specific capacity and long-term performance. The specific capacity values of the SCs are provided in **Figure 9**a. The term "specific capacity" denotes the amount of electrochemical energy an electrochemical material can store per unit mass, typically measured in mAh/g. The specific capacity of the material is analyzed in SI Figure S-GCPL[†], considering various current densities ranging from 0.1 to 2.4 A/g. A relationship exists between the specific capacity and the current density; a lower current density is associated with a higher specific capacity value.[43] Increasing current density could speed up the charging and discharging rate in the electrode material. Still, at the same time, it can diminish the energy-storage capacity due to incomplete electrochemical reactions during faster charge/discharge cycles, leading to energy dissipation.

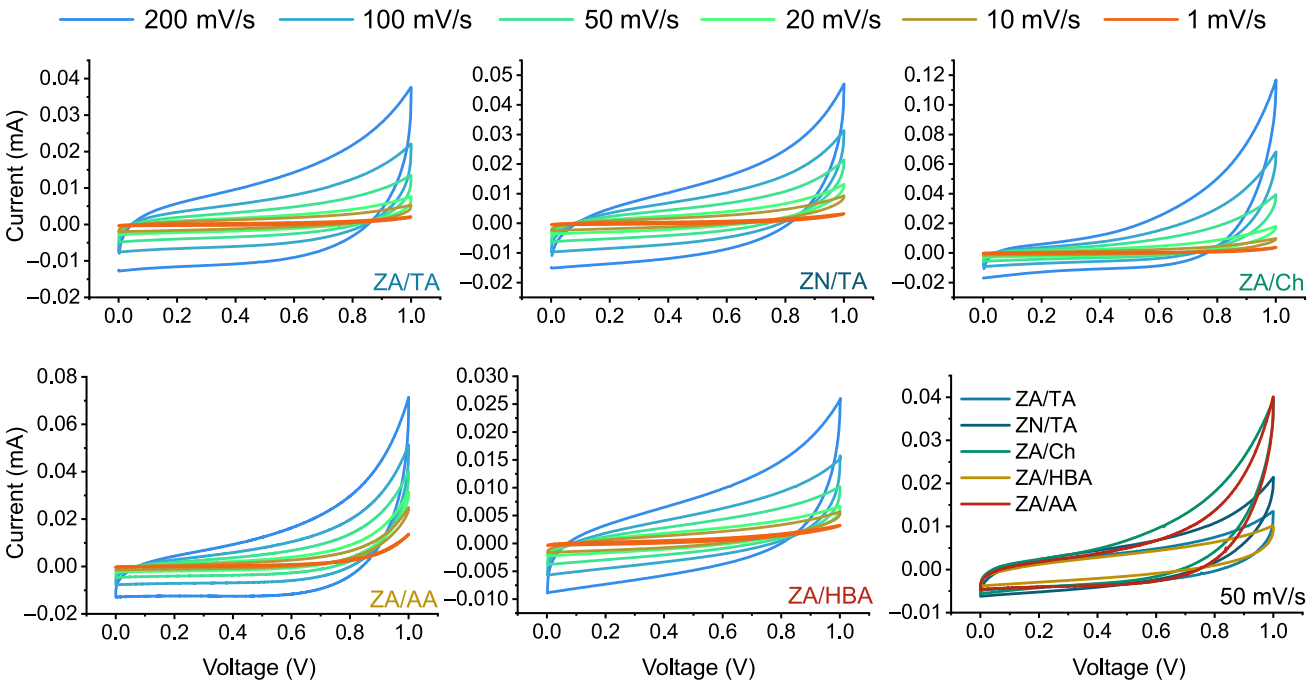

Figure 7. Cyclic voltammetry (CV) curves of the ZnO-based supercapacitor SC devices measured at different scan rates, and a comparison of the CV curves obtained at 50 mV/s for each material.

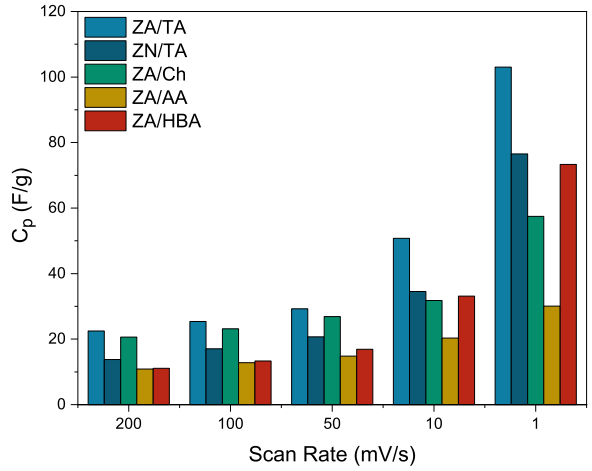

Figure 8. Specific capacity values of the supercapacitor devices using ZnO electrode materials as a function of the scan rate.

Consequently, the energy stored per unit mass decreases as the current density increases.[64,65] The optimal current density for GCPL was determined to be 0.1 A/g. The specific capacity values of the designed SCs at a current density of 0.1 A/g can be observed in Figure 9a. The SC design that exhibited the highest energy-storage capacity used ZA/TA as an electrode material, with an approximate value of 0.04 mAh/g.

The long-term usage of the ZnO-based SCs has been evaluated after 10,000 charge/discharge cycles by evaluating the Coulombic efficiency (Figure 9b) and capacitance retention (Figure 9c) values. All designs exhibit Coulombic effectiveness exceeding 98.5% and demonstrate consistent stability. The electrical charge loss remains nearly constant throughout the first charge/discharge cycle, with little or no loss. Capacitance retention relates to the capacity of an energy-storage system at any given time during its lifespan compared to its original capacity. After 10,000 cycles, all samples, except for ZA/AA, exhibited values close to their original capacity, demonstrating a capacitance retention rate exceeding 98 percent.

Table II summarizes the SCs' specific capacitance, energy, and power density parameters calculated based on the equations presented in the SI file†. The utilization of various capping agents during the production of ZnO NPs had an important effect on the electrochemical characteristics of the designed SCs. Among the critical parameters that could affect the material's electrochemical characteristics is the impact of the capping agent on surface morphologies; differently sized and shaped ZnO NPs are produced by each capping agent.

ZnO nanoparticles are mainly functionalized by capping agents such as TA, Ch, AA, and HBA. Each agent selectively adds particular functional groups to the ZnO particles' surface, causing substantial changes in their chemical and physical characteristics. As it was observed in other studies, because of its carboxylic acid groups, TA can increase porosity[66] and form rod-shaped structures,[67] which are advantageous for electrochemical operation. The biopolymer Ch incorporates amino and hydroxyl groups that can interact with metal ions,[68] potentially enhancing its storage capacity. The reduction and stability of nanoparticles are facilitated by AA[69] and HBA,[70] wherein the size and surface characteristics of the particles are influenced by their functional groups.

Accordingly, it is seen that the ZA/TA and ZN/TA in which tartaric acid was utilized in this work as the structure-directing agent to change the surface of ZnO particles exhibit rod-like structures with large porosity between the grains, regardless of the zinc source used. The presence of large pores promotes electrochemical reactions in highly active regions, leading to enhanced reaction kinetics and ion/electron-transport rates. The SC design utilizing ZA/TA as the electrode material had the highest specific capacitance value, calculated at 103 F/g. Furthermore, the measurements revealed energy and power density values of 14.3 Wh/kg and 167 kW/kg, respectively.

Tartaric acid, a carboxylic acid with a structure that includes double bonds and carboxylic acid groups, is believed to induce a porous structure within the zinc oxide nanoparticles. Acetic acid, a simpler carboxylic acid with fewer carboxylic groups, did not contribute significantly to porosity. The presence of more carboxylic acid groups (−COOH) has been linked to greater gelation. Because of their high reactivity, as the temperature increases, they shatter into small pieces and form weblike polymer groups, increasing the viscosity and, thus, gelation. Although ascorbic acid lacks carboxylic groups, its enediol structure, along with the benzene rings in hydroxybenzoic acids, was observed to reduce the size of the nanoparticles.

Further, it was noted that the carboxylic groups of tartaric acid and its unique double-bond configuration enhanced the gelation process, resulting in zinc oxide nanoparticles with porous and rod-like structures. Low concentrations of tartaric acid led to the formation of a petal-like nanoparticle structure, while higher concentrations favored rod-like and porous structures. It was proven that this porous structure promotes the electrochemical reaction frequency and, thus, the electrochemical performance of ZnO nanoparticles.[34]

Many studies have analyzed the ability of ZnO as an electrode for SCs, observing that ZnO is an efficient electrode material.[17,43,71] It is all due to the remarkable properties of ZnO, like broad bandgap, many defects, and high electron mobility, making it a promising material for SCs. Nanoscale ZnO has different electrical-transport properties than the bulk ZnO counterpart, mainly due to the existence of defect centers. Such electrical-transport properties of defects in ZnO nanocrystals have been presented earlier by EPR and two-point DC electrical results.[71] Repp et al. reported that the specific resistivity of ZnO is reduced drastically with decreasing

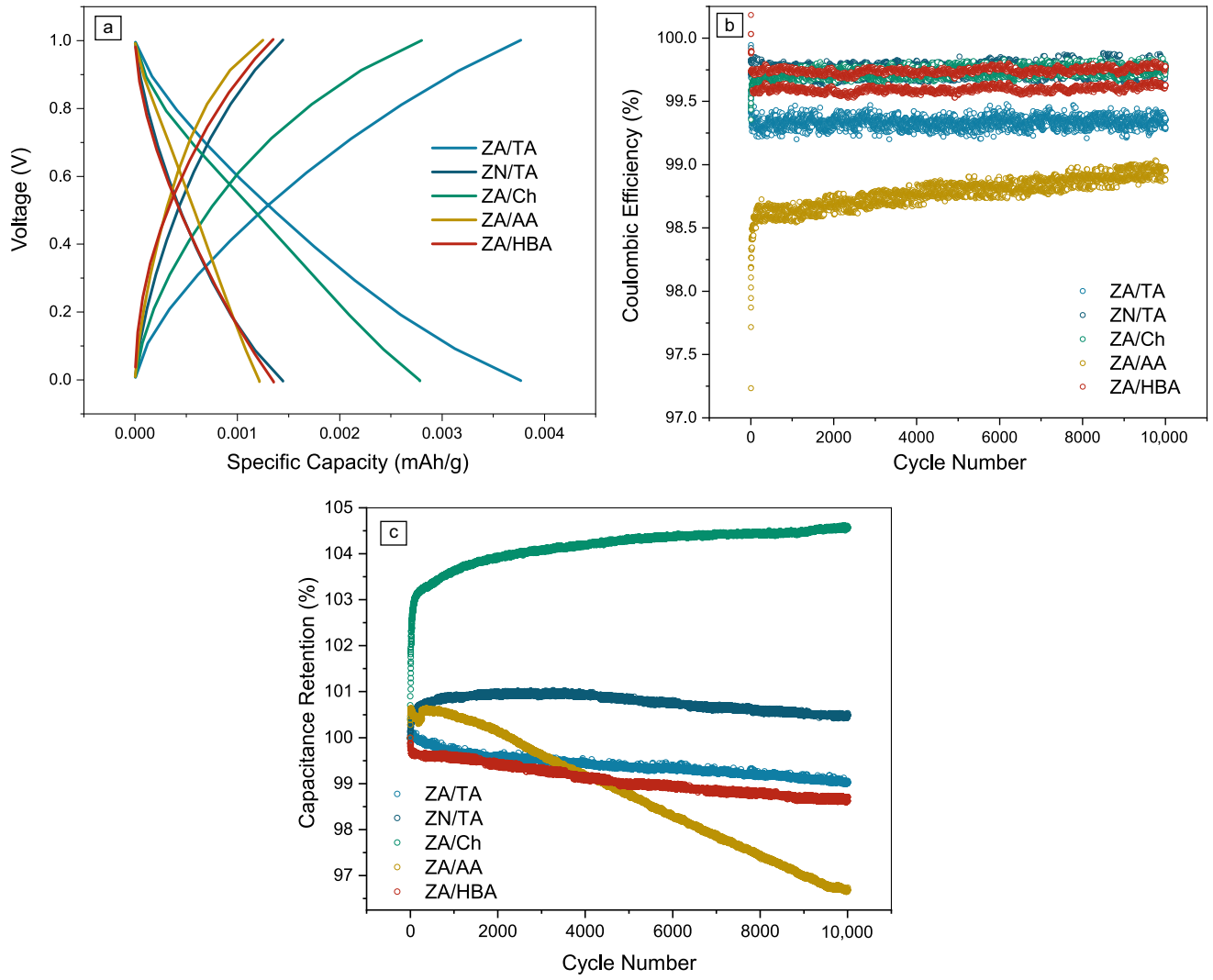

Figure 9. Specific capacity C_P versus voltage measurements (a), long-term stability evaluation by Coulombic efficiency (b), and capacitance retention (c) of all supercapacitor devices based on the different ZnO materials.

Table II. Specific capacity (C_P), energy (E_D), and power (P_D) density of the symmetric SCs based on ZnO nanoparticles as electrode materials.

Design	C_P F/g	E_D Wh/kg	P_D kW/kg
ZA/TA	103.1	14.3	167.0
ZN/TA	76.5	10.6	190.0
ZA/Ch	57.5	8.0	80.1
ZA/AA	30.1	4.2	61.8
ZA/HBA	73.3	10.2	272.4

the crystallite size, thus increasing the concentration of surface defects.[72]

As summarized in **Table III**, a marked improvement in the electrochemical performance can be observed, underscored by the specific capacitance values. These values have been found to outperform those reported in the literature. The performance leap has been attributed to the strategic incorporation of capping reagents and carbon-defect centers, which effectively enhance the electrochemical characteristics of the materials. Remarkably, this significant uptick in specific capacitance was realized without conventional "booster" materials. Typically, additives such as carbon aerogel, activated carbon, and graphene amplify electrochemical performance. The fact that these additives were not used in the study highlights the effectiveness of the capping agents and the carbon-defect centers.

Furthermore, the findings demonstrate not only incremental but substantial advancements in energy and power densities compared to those documented in the existing literature. The critical metric of energy density, determining

Table III. Different ZnO-based electrode materials used in SC devices already reported in the literature.

Electrode	C_P / F/g	References
ZA/TA	103.1	t.w.
ZN/HBA	73.3	t.w.
$ZnFe_2O_4$/CC	66.3	73
ZnO/AC	68.2	74
C/ZnO	25	75
CNT/ZnO	59	76
GR/ZnO	61.7	77
ZnOSS/rGO@Ni	31	78

t.w. = this work

the total amount of energy that can be stored in a given system, and power density, reflecting how quickly that energy can be delivered or discharged, have seen significant improvements.

Conclusions

This study obtained ZnO materials employing different capping agents such as tartaric acid, chitosan, ascorbic acid, and 4-hydroxybenzoic acid. Morphostructural studies showed that the materials were of high purity and crystallinity, with average crystallite sizes smaller than 100 nm. Raman and EPR spectroscopy evidenced the presence of carbon dopants in the materials introduced by the used capping agents. Low- and high-field EPR measurements, along with PL spectroscopy, highlighted the paramagnetic and nonparamagnetic defect centers present in the carbon-doped ZnO, which have a greater influence on the electric properties evaluated in symmetric supercapacitor devices, resembling promising results. The best specific capacity values (103.1 F/g), energy (14.3 Wh/kg), and power density (167 kW/kg) were obtained for the supercapacitor device that used tartaric acid as a capping agent. All supercapacitor devices had capacity retention above 98% even after 10,000 charge–discharge cycles, showing suitability for long-term usage.

Author contributions

E.E.: Formal analysis, Investigation, Writing—Original Draft, and Writing—Review and Editing; S.E.: Formal analysis, Investigation, Writing—Original Draft, Writing—Review and Editing, and Visualization; M.O.: Investigation; F.B.M.: Methodology, Formal analysis, Investigation, Writing—Original Draft, and Visualization; A.G.: Validation, Formal analysis, Investigation, Writing—Original Draft, and Writing—Review and Editing; A.O.: Investigation; F.K.: Methodology and Writing—Original Draft; A.M.R.: Conceptualization, Methodology, Validation, Formal analysis, Investigation, Data Curation, Writing—Original Draft, Writing—Review and Editing, Visualization, and Supervision; C.K.: Conceptualization, Validation, Formal analysis, Writing—Original Draft, Writing—Review and Editing, and Supervision; and E.E.: Conceptualization, Validation, Formal analysis, Data Curation, Writing—-Original Draft, Writing—Review and Editing, and Supervision.

Funding

This work was supported through the Core Program within the National Research Development and Innovation Plan 2022–2027, carried out with the support of Ministerul cercetarii, inovarii si dezvoltarii (MCID), Project No. 27N/03.01.2023, component Project Code PN 23 24 01 03. A portion of this work was performed at the National High Magnetic Field Laboratory, which is supported by the National Science Foundation Cooperative Agreement No. DMR-2128556 and the State of Florida.This work was supported through the Core Program within the National Research Development and Innovation Plan 2022–2027, carried out with the support of Ministerul cercetarii, inovarii si dezvoltarii (MCID), Project No. 27N/03.01.2023, component Project Code PN 23 24 01 03. A portion of this work was performed at the National High Magnetic Field Laboratory, which is supported by the National Science Foundation Cooperative Agreement No. DMR-2128556 and the State of Florida.

Data availability

The authors confirm that the data supporting the findings of this study are available within the article and its supplementary materials.

Code availability

Not applicable.

Conflict of interest

The authors declare that they have no known competing financial interests or personal relationships that could have appeared to influence the work reported in this article.

Supplementary information

The online version contains supplementary material available at https://doi.org/10.1557/s43577-024-00845-z.

Open Access

References

1. B. Üstün, H. Aydın, S.N. Koç, Ü. Kurtan, *Diam. Relat. Mater.* **136**, 110048 (2023)
2. L. Qin, J. Jiang, Q. Tao, C. Wang, I. Persson, M. Fahlman, P.O. Persson, L. Hou, J. Rosen, F. Zhang, *J. Mater. Chem. A* **8**(11), 5467 (2020)
3. X. Zhao, B.M. Sánchez, P.J. Dobson, P.S. Grant, *Nanoscale* **3**(3), 839 (2011)
4. M.I.A. Abdel Maksoud, R.A. Fahim, A.E. Shalan, M. Abd Elkodous, S.O. Olojede, A.I. Osman, C. Farrell, A.A.H. Al-Muhtaseb, A.S. Awed, A.H. Ashour, D.W. Rooney, *Environ. Chem. Lett.* **19**, 375 (2021)
5. E. Serrano, G. Rus, J. Garcia-Martinez, *Renew. Sustain. Energy Rev.* **13**(9), 2373 (2009)
6. Z. Li, J. Bu, C. Zhang, L. Cheng, D. Pan, Z. Chen, M. Wu, *New J. Chem.* **45**(24), 10672 (2021)
7. W. Wang, S. Jiao, J. Cao, H.E. Naguib, *Electrochim. Acta* **350**, 136353 (2020)
8. S. Shi, X. Zhuang, B. Cheng, X. Wang, *J. Mater. Chem. A* **1**(44), 13779 (2013)
9. M.M. Ba-Abbad, A.A.H. Kadhum, A.B. Mohamad, M.S. Takriff, K. Sopian, *J. Alloys Compd.* **550**, 63 (2013)
10. M. Biji, M.I. Irfana, S. Sreejamol, P. Shajesh, S. Ananthakumar, R.V. Mangalaraja, S. Anas, *Mater. Today Proc.* **9**, 560 (2019)
11. M.R. Pallavolu, J. Nallapureddy, R.R. Nallapureddy, G. Neelima, A.K. Yedluri, T.K. Mandal, B. Pejjai, S.W. Joo, *J. Alloys Compd.* **886**, 161234 (2021)
12. N. Kondal, *Mater. Today Proc.* **37**, 3056 (2021)
13. C. Abed, M.B. Ali, A. Addad, H. Elhouichet, *Mater. Res. Bull.* **110**, 230 (2019)
14. A. Tabib, W. Bouslama, B. Sieber, A. Addad, H. Elhouichet, M. Férid, R. Boukherroub, *Appl. Surf. Sci.* **396**, 1528 (2017)
15. G. Guo, Z. Zhou, J. Li, H. Yan, F. Li, *Molecules* **26**(12), 3554 (2021)
16. S. Xu, Z.L. Wang, *Nano Res.* **4**, 1013 (2011)
17. C.T. Altaf, A.M. Rostas, M. Mihet, M.D. Lazar, I. Iatsunskyi, E. Coy, E. Erdem, M. Sankir, N.D. Sankir, *J. Mater. Chem. C* **10**(29), 10748 (2022)
18. A.U. Ammar, I.D. Yildirim, M.H. Aleinawi, M. Buldu-Akturk, N.S. Turhan, S. Nadupalli, A.M. Rostas, E. Erdem, *Mater. Res. Bull.* **160**, 112117 (2023)
19. M. Siddique, N. Fayaz, M. Saeed, *Physica B Condens. Matter* **602**, 412504 (2021)
20. K. Sowri Babu, A. Ramachandra Reddy, C. Sujatha, K. Venugopal Reddy, A. Mallika, *J. Adv. Ceram.* **2**, 260 (2013)
21. R. Mahdavi, S.S.A. Talesh, *Ultrason. Sonochem.* **39**, 504 (2017)
22. B.E. Conway, *Electrochemical Supercapacitors: Scientific Fundamentals and Technological Applications* (Springer, Cham, 2013)
23. L.L. Zhang, X. Zhao, *Chem. Soc. Rev.* **38**(9), 2520 (2009)
24. J.R. Miller, P. Simon, *Science* **321**(5889), 651 (2008)
25. L. Qin, J. Jiang, L. Hou, F. Zhang, J. Rosen, *Energy Environ. Mater.* **7**(4), e12653 (2023)
26. V. Vimala, L. Cindrella, *Chem. Phys. Lett.* **809**, 140172 (2022)
27. R. Shakil, M.N. Shaikh, S.S. Shah, A.H. Reaz, C.K. Roy, A.N. Chowdhury, M.A. Aziz, *Asian J. Org. Chem.* **10**(8), 2220 (2021)
28. A. Bronusiene, A. Popov, I. Barauskiene, I. Ancutiene, *Surf. Interfaces* **25**, 101275 (2021)
29. G. Bhanjana, G.R. Chaudhary, N. Dilbaghi, A. Kaushik, K.H. Kim, S. Kumar, *Mater. Today Chem.* **26**, 101142 (2022)
30. S. Raha, M. Ahmaruzzaman, *Nanoscale Adv.* **4**(8), 1868 (2022)
31. E.D. Glendening, R. Faust, A. Streitwieser, K.P.C. Vollhardt, F. Weinhold, *J. Am. Chem. Soc.* **115**(23), 10952 (1993)
32. Z. Wang, C. Du, S. Lei, D. Ding, R. Chen, S. Yang, T. Cai, *J. Mater. Chem. A* **9**(46), 25796 (2021)
33. R. Vinodh, Y. Sasikumar, H.-J. Kim, R. Atchudan, M. Yi, *J. Ind. Eng. Chem.* **104**, 155 (2021)
34. S. Suwanboon, P. Amornpitoksuk, C. Randorn, *Ceram. Int.* **45**(2), 2111 (2019)
35. G. Wang, Y. Liu, X. Dong, X. Zhang, *J. Hazard. Mater.* **437**, 129357 (2022)
36. C.H. Foyer, "Ascorbic Acid," in *Antioxidants in Higher Plants* (CRC Press, Boca Raton, 2017), pp. 31–58
37. J. Teixeira, C. Oliveira, R. Amorim, F. Cagide, J. Garrido, J.A. Ribeiro, C.M. Pereira, A.F. Silva, P.B. Andrade, P.J. Oliveira, F. Borges, *Sci. Rep.* **7**(1), 6842 (2017)
38. K.P. Raj, K. Sadayandi, *Physica B Condens. Matter* **487**, 1 (2016)
39. M. Deepty, C. Srinivas, E.R. Kumar, N.K. Mohan, C.L. Prajapat, T.C. Rao, S.S. Meena, A.K. Verma, D.L. Sastry, *Ceram. Int.* **45**(6), 8037 (2019)
40. J. Ungula, B. Dejene, *Physica B Condens. Matter* **480**, 26 (2016)
41. A. Savoyant, M. Rollo, M. Texier, R.E. Adam, S. Bernardini, O. Pilone, O. Margeat, O. Nur, M. Willander, S. Bertaina, *Nanotechnology* **31**(9), 095707 (2019)
42. M. Toufani, S. Kasap, A. Tufani, F. Bakan, S. Weber, E. Erdem, *Nanoscale* **12**(24), 12790 (2020)
43. A.U. Ammar, F. Bakan-Misirlioglu, M.H. Aleinawi, G. Franzo, G.G. Condorelli, F.N.T. Yesilbag, Y.O. Yesilbag, S. Mirabella, E. Erdem, *Mater. Res. Bull.* **165**, 112334 (2023)
44. C.T. Altaf, T.O. Colak, A.M. Rostas, M. Mihet, M.D. Lazar, I. Iatsunskyi, E. Coy, I.D. Yildirim, F.B. Misirlioglu, E. Erdem, M. Sankir, *J. Energy Storage* **68**, 107694 (2023)
45. E. Erdem, *J. Alloys Compd.* **605**, 34 (2014)
46. C.H. Ahn, Y.Y. Kim, D.C. Kim, S.K. Mohanta, H.K. Cho, *J. Appl. Phys.* **105**(1), 013502 (2009)
47. P. Jakes, E. Erdem, *Phys. Status Solidi Rapid Res. Lett.* **5**(2), 56 (2011)
48. S. Nadupalli, S. Repp, S. Weber, E. Erdem, *Nanoscale* **13**(20), 9160 (2021)
49. H. Kaftelen, K. Ocakoglu, R. Thomann, S. Tu, S. Weber, E. Erdem, *Phys. Rev. B* **86**(1), 014113 (2012)
50. M. Kakazey, M. Vlasova, V. Gómez-Vidales, A. Ángeles-Pascual, V. Basiuk, *Phys. Chem. Chem. Phys.* **19**(5), 3670 (2017)
51. M. Kakazey, M. Serrano, M. Vlasova, V.A. Basiuk, E.V. Basiuk, V. Gómez-Vidales, P.J. Sebastian, *J. Alloys Compd.* **762**, 605 (2018)
52. M. Kakazey, M. Vlasova, E.A. Juarez-Arellano, *J. Nanopart. Res.* **17**(3), 118 (2015)
53. V. Vivier, M.E. Orazem, *Chem. Rev.* **122**(12), 11131 (2022)
54. K.B. Li, D.W. Shi, Z.Y. Cai, G.L. Zhang, Q.A. Huang, D. Liu, C.P. Yang, *Electrochim. Acta* **174**, 596 (2015)
55. S. Zhao, F. Wu, L. Yang, L. Gao, A.F. Burke, *Electrochem. Commun.* **12**(2), 242 (2010)
56. M.Ö.A. Çolak, A. Güngör, M.B. Akturk, E. Erdem, R. Genç, *Nanoscale* **16**(2), 719 (2024)
57. A. Güngör, F. Bakan-Misirlioglu, R.G. Alturk, E. Erdem, *J. Energy Storage* **76**, 110143 (2024)
58. T.H. Wu, D. Hesp, V. Dhanak, C. Collins, F. Braga, L.J. Hardwick, C.C. Hu, *J. Mater. Chem. A* **3**(24), 12786 (2015)
59. A. Güngör, S.G. Çolak, M.Ö.A. Çolak, R. Genç, E. Erdem, *Electrochim. Acta* **480**, 143924 (2024)
60. Q. Li, M. Haque, V. Kuzmenko, N. Ramani, P. Lundgren, A.D. Smith, P. Enoksson, *J. Power Sources* **348**, 219 (2017)
61. X. Pu, D. Zhao, C. Fu, Z. Chen, S. Cao, C. Wang, Y. Cao, *Angew. Chem. Int. Ed.* **60**(39), 21310 (2021)
62. M.F. Dupont, S.W. Donne, *J. Power Sources* **326**, 613 (2016)
63. A. Hauch, A. Georg, *Electrochim. Acta* **46**(22), 3457 (2001)
64. K.G. Gallagher, S.E. Trask, C. Bauer, T. Woehrle, S.F. Lux, M. Tschech, P. Lamp, B.J. Polzin, S. Ha, B. Long, Q. Wu, *J. Electrochem. Soc.* **163**(2), A138 (2015)
65. J. Zhang, D.W. Wang, W. Lv, S. Zhang, Q. Liang, D. Zheng, F. Kang, Q.H. Yang, *Energy Environ. Sci.* **10**(1), 370 (2017)
66. Y. Qin, K. Zhang, X. He, *J. Clean. Prod.* **337**, 130477 (2022)
67. R.S. Rai, V. Bajpai, *Adv. Nano Res.* **11**(1), 37 (2021)
68. E. Guibal, *Sep. Purif. Technol.* **38**(1), 43 (2004)
69. Y. Qin, X. Ji, J. Jing, H. Liu, H. Wu, W. Yang, *Colloids Surf. A Physicochem. Eng. Asp.* **372**(1–3), 172 (2010)
70. A. Aji, S.J. Santosa, E.S. Kunarti, *Indones. J. Chem.* **20**(2), 413 (2020)
71. S. Parashar, B. Murty, S. Repp, S. Weber, E. Erdem, *J. Appl. Phys.* **111**, 11 (2012)
72. S. Repp, E. Erdem, *Spectrochim. Acta A Mol. Biomol. Spectrosc.* **152**, 637 (2016)
73. S. Polat, *Türk Doğa ve Fen Dergisi* **10**(2), 199 (2021)
74. M.S. Yadav, A. Sinha, M. Singh, *Mater. Res. Express* **5**(8), 085503 (2018)
75. D. Kalpana, K. Omkumar, S.S. Kumar, N. Renganathan, *Electrochim. Acta* **52**(3), 1309 (2006)
76. L. Aravinda, K. Nagaraja, H. Nagaraja, K.U. Bhat, B.R. Bhat, *Electrochim. Acta* **95**, 119 (2013)
77. T. Lu, Y. Zhang, H. Li, L. Pan, Y. Li, Z. Sun, *Electrochim. Acta* **55**(13), 4170 (2010)
78. A. Kumar, R. Adalati, M. Sharma, N. Choudhary, K.S. Kumar, L. Hurtado, Y. Jung, Y. Kumar, J. Thomas, R. Chandra, *Mater. Today Commun.* **34**, 105362 (2023)